Comprehensive investigation of microstructure, electrical and photocatalytic properties of K$_{0.5}$Na$_{0.5}$NbO$_3$ lead- free ceramics prepared via different synthesis routes

Manish Saha[1,2], Phyu Phyu Cho[3], Ch. Subrahmanyam[3], Manish K. Niranjan[2,*], and Saket Asthana[1,*]

[1] *Advanced Functional Materials Laboratory, Department of Physics, Indian Institute of Technology, Hyderabad 502284, India*

[2] *Theoretical Nanoscience Group, Department of Physics, Indian Institute of Technology, Hyderabad 502284, India*

[3] *Department of Chemistry, Indian Institute of Technology, Hyderabad 502284, India*

ABSTRACT

The comprehensive study on the impact of different synthesis techniques on the structural, electrical, and photocatalytic properties of perovskite ferroelectric ceramics K$_{0.5}$Na$_{0.5}$NbO$_3$(KNN). The solid-state reaction and hydrothermal methods are used to prepare the KNN ceramics, and the effects of grain size on the physical characteristics these ceramics are examined. The KNN-S prepared by solid-state method have significantly larger grain size as compared to that for KNN-H prepared by hydrothermal method. Furthermore, the KNN-S is found to exhibit higher dielectric, piezoelectric and ferroelectric properties as compared to KNN-H. On the other hand, the increased photocatalytic activity is observed in KNN-H as compared to KNN-S. As compared to the hydrothermal synthesis, the solid-state synthesis causes an increase in the relative dielectric permittivity (ϵ') from 2394 to 3286, remnant polarization (P_r) from 15.38 to 20.41 μC/cm^2, planer electromechanical coupling factor $\left(k_p\right)$ from 0.19 to 0.28 and piezoelectric coefficient (d_{33}) from 88 to 125 pC/N. The KNN-S ceramics are also found to have a lower leakage current density, and higher grain resistance than KNN-H ceramic. The enhanced photocatalytic activity of KNN-H is attributed to relatively smaller particle sizes. The KNN-S and KNN-H samples are found to have degradation efficiencies of RhB solution of 20% and 65%, respectively. The study highlights the importance of synthesis methods and how these can be exploited to tailor the dielectric, piezoelectric and photocatalytic properties of KNN.

Address correspondence to E-mail: manish@phy.iith.ac.in; asthanas@phy.iith.ac.in

1 Introduction

Piezo/ferro-electric ceramics are important class of materials with enormous applications in electrical devices such as sensors, transducers and actuators [1]. In particular, $Pb(Zr_{1-x}Ti_x)O_3$ or PZT based ceramics have long dominated the piezoelectric device industries due to their excellent piezoelectric properties ($d_{33} = 410$ pC/N, $k_p = 0.60$) [2]. However, over the years, the toxic nature of lead in these materials have raised enormous concern for environment and human health. This has led to vigorous push for search and development of high performance lead-free piezo/ferroelectrics as substitute for PZT [3].

Among the potential materials, the lead-free piezoelectric sodium potassium niobate ((K, Na)NbO$_3$, hereafter KNN) based materials have been found highly promising with potential to replace lead-based piezoelectric materials because of their piezoelectric properties ($d_{33} = 171 - 490$ pC/N, $k_p \sim 0.64$) and high Curie temperature ($T_c = 178 - 475\,°C$) [4–6]. Solid solutions of antiferroelectric NaNbO$_3$ and ferroelectric KNbO$_3$ constitute the KNN ceramic. It has been suggested that KNN system possesses the best piezoelectric, ferroelectric and electromechanical properties when the K/Na ratio is near to 50/50 [7]. Among the KNN compositions, the $K_{0.5}Na_{0.5}NbO_3$ has received the most of the attention due to its superior ferroelectric and piezoelectric properties over the other compositions along with a high Curie temperature around 420 °C [8] and low coercive field of 11.52 kV/cm [9]. $K_{0.5}Na_{0.5}NbO_3$ ceramic undergoes three distinct phase transitions from high to low temperature: cubic to tetragonal (Curie temperature), tetragonal to orthorhombic (≈ 210 °C), orthorhombic to rhombohedral ($\approx$ -123 °C) [4].

The interest in KNN as photocatalytic agent stems from the concern over organic dye wastes as environmental pollutants from the textile industries. Though these water pollutants have grown over several years, there hasn't been much progress made to remove them [10]. Although several chemical treatment methods are used to remove dangerous elements from dye wastewater, not all of them are completely effective in degrading organic colours. In particular, Rhodamine-B (RhB) is one of the hardest dyes to break because of its complex structures. Thus, development of simple and cost-effective wastewater treatment methods is highly desirable [11]. In recent years, a phenomenon known as "Photocatalysis"

has been found to be quite promising as a potential method to eliminate harmful substances from wastewater without producing secondary contamination [12]. As the primary difficulty in photocatalysis is the recombination of photoexcited electrons and holes, the separation of electrons and holes produced by the internal field in ferroelectric crystals prevents charge carrier recombination, which increases the duration of the photocatalytic activity [13]. This makes ferroelectric materials very promising candidates for their use as photocatalysts. However, not many ferroelectrics have been explored as photocatalysts [14–16]. In addition, it is also worth exploring that how particle or grain size of the ferroelectric material impacts the photocatalysis process. It is generally known that the response efficiency of smaller particles is higher due to high availability of active surface sites. The physical properties may also be expected to depended on factors such as microstructure, which in turn may depend on different synthesis methods. Therefore, it is important to understand as to how different synthesis processes affect physical properties. Thus, different preparation techniques present an opportunity to enhance and tailor the physical properties via engineering grain size or microstructure [17–20].

The synthesis of pure KNN via solid-state reactions [21, 22], hydrothermal processes [23, 24], sol-gel techniques [25, 26] and solution routes [27, 28] has been reported over the years. However, studies that explore the correlation between the electrical characteristics and various synthesis methods of KNN are scarce [29, 30]. Additionally, the impact of grain size on electrical characteristics have received minimal consideration in case of KNN system [31–34]. This may have been due to the difficulty in producing KNN ceramics with various grain sizes. It may be noted that optimisation of the sintering temperature is a critical and challenging issue with KNN ceramics for a number of reasons [35]. This renders the synthesis of dense sintered KNN ceramics quite difficult. KNN-based ceramics prepared by spark plasma sintering and hot-pressed sintering have been reported to achieve the necessary densification [36, 37]. Although these techniques can produce KNN ceramics with higher densities and piezoelectric capabilities (($d_{33} = 160$ pC/N, via hot-pressed sintering [36]) than those made via the solid-state reaction ($d_{33} = 96$ pC/N) [38], nevertheless these (techniques) are not suitable for mass production of KNN. The pressure-less or conventional sintering of

these materials is more appropriate for large scale production.

Therefore, in this work, we present a comparative study of structural, dielectric, piezoelectric / ferroelectric and photocatalytic properties of KNN synthesised using a conventional solid-state procedure and a hydrothermal approach. In our study, the hydrothermal method is also chosen along with the solid-state technique since it offers advantages such as uniformity in compositions, stoichiometry and lower sintering temperature. Our results suggest that these two synthesis methods influence the grain size, that in turn affects relative dielectric permittivity, ferroelectric polarisation and impedance of the KNN. We also explore the efficacy of KNN as a potential photocatalytic material and the impact of different synthesis methods on its photocatalytic properties. Because of the higher calcination temperature, the particles obtained by the solid-state process are generally larger in size as compared to powder obtained using the hydrothermal method. The efficiency and photocatalytic activity of the two types of samples are found to display noticeable variation.

2 Experimental details

2.1 Synthesis of materials

$K_{0.5}Na_{0.5}NbO_3$ ceramics are prepared using two separate synthesis procedures: a conventional solid-state method and a hydrothermal method. The samples prepared by these methods are indicated as KNN-S and KNN-H, respectively. High purity precursors such as K_2CO_3 (99.99% Sigma Aldrich Chemicals, USA), Na_2CO_3 (99.5% Sigma Aldrich Chemicals, USA) and Nb_2O_5 (99.99% Sigma Aldrich Chemicals, USA) are used to prepare compounds for the synthesis of KNN-S. Stoichiometric proportions of powders are mixed using agate mortar pestle and grounded manually for 10 h using Isopropyl alcohol (IPA) as a medium. Thereafter, the combined powder is calcined for 3 h in an environment of air at 850 °C.

In case of hydrothermal synthesis, the KOH (85% Sigma Aldrich Chemicals, USA), NaOH (97% Sigma Aldrich Chemicals, USA) and Nb_2O_5 powders are used as the starting materials. First, 70 mL of deionized (DI) water is used to dissolve KOH with a weight equivalent to 10 M concentration. Then, a specific proportion of Nb_2O_5 is added with KOH solution in accordance with the final composition of $KNbO_3$ solution and the mixture are magnetically stirred until a homogenous white solution formed. The mixture is transferred into a 100 mL Teflon vessel. The same procedure is followed to make $NaNbO_3$ solution by using NaOH instead of KOH precursor. Teflon vessel of $KNbO_3$ and $NaNbO_3$ solutions is placed in the autoclave and heated at 210 °C under automatically produced pressure for 24 h. The autoclave is thereafter allowed to naturally cool to ambient temperature. The resultant powders are rinsed several times with deionized water until the pH level of the solution becomes neutral. Thereafter, the solution is heated at 100 °C temperature for 120 min to obtain as-synthesized $KNbO_3$ and $NaNbO_3$ powders. $KNbO_3$ and $NaNbO_3$ powders were mixed in a molar ratio of 1:1 to synthesize $K_{0.5}Na_{0.5}NbO_3$ ceramic. To achieve the to $NaNbO_3$ molar ratio of 1 in the ceramics, the amounts were 0.523 g and 0.476 g respectively. Then, this powder was ground with alumina mortar and pestle; finally, $K_{0.5}Na_{0.5}NbO_3$ powders are prepared for characterizations. The Fig. 1 shows a schematic diagram of the hydrothermal synthesis process. The resulting calcined powders from solid-state and hydrothermal synthesis are further grounded and combined with polyvinyl alcohol (PVA, 5 wt%) as a binder. Thereafter, the powders are compressed into a circular pellet (diameter = 8 mm) by applying 4 Ton hydraulic pressure. Finally, the KNN-S and KNN-H pellets are sintered in a closed alumina crucible at optimized conditions of 1100 °C for 4 h and 1025 °C for 6 h, respectively, with heating and cooling rates of 2 °C/min. Since potassium is a volatile element, all pellets are covered with their equivalent calcined powders throughout the sintering process to prevent volatilization of potassium and sodium elements. Energy Dispersive Spectroscopy (EDS), as indicated in the supplementary file, confirms the compositional distribution of the elements.

2.2 Characterization of materials

The phase formation study is performed using a powder X-ray diffractometer (Rigaku, SmartLab) with a nickel filter for Cu-Kα radiation (λ_1 = 1.544 Å, λ_2 = 1.541 Å) at room temperature where 2θ angle ranges from the 20° to 80° with the step size of 0.0168 (2θ) and at a scan rate of 2 °/min. The Archimedes approach is used to determine the apparent density. Where, deionized water is used as the immersion liquid. The surface morphology of sintered pellets is observed via

Fig. 1 Schematic diagram of the hydrothermal process of KNbO$_3$ and NaNbO$_3$ synthesis
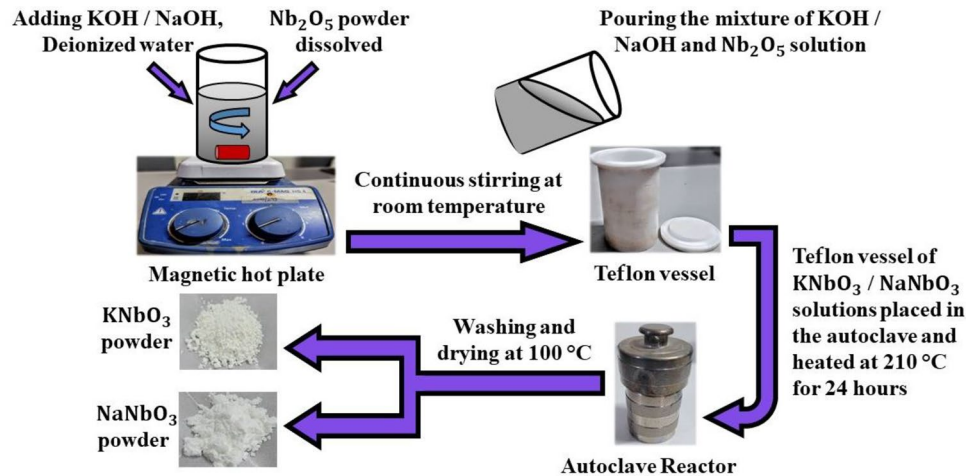
scanning electron microscopy (SEM) (Zeiss, Supra 40) at an acceleration voltage of 10 kV, where a thin layer of gold sputtering is used to electrode the samples. For further electrical measurements, silver paste is fired on both sides of the samples at 200 °C for 2 h to form the electrodes.

Then temperature dependence dielectric and impedance studies at different frequencies are carried out using an impedance analyzer (Wayne Kerr 6500B) in the temperature range of 30–500 °C with the heating rate of 3 °C/min; where the temperature controlling equipment used for dielectric and impedance measurements is Eurotherm. A range of frequencies between 1 kHz and 1 MHz are used to measure the temperature dependence of the relative dielectric permittivity (ϵ') and dielectric loss (tanδ). The impendence data are analysed using the resonance and anti-resonance method in order to calculate the planer electromechanical coupling factor (k_p). The parameters such as Polarization (P), switching current (I) and leakage current density (J) as a function of applied electric field are measured at room temperature using TF-Analyzer 2000 (aixACCT systems, GmbH) at 1 Hz frequency. The piezoelectric coefficient (d_{33}) is determined at room temperature using a quasi-static metre (Piezotest, PM300). The Perkin-Elmer Lambda 1050 UV(Ultraviolet)/Vis(Visible)/NIR(near-infrared) spectrophotometer is used to measure Ultraviolet–Visible (UV–Vis) diffuse reflectance spectra. BET(Brunauer–Emmett–Teller) analyzer (Quantachrome, NOVA 2200e) is used to measure the surface area.

Photocatalytic activity of KNN-S and KNN-H powders is estimated by degrading rhodamine B (RhB) dye (Merck, with assay of ≥ 97.0%) under visible light irradiation using the halogen lamp (500 W). For each sample, 50 mL of 10 mg/L dye solution is mixed with 0.25 g of KNN. Before exposure to the light source, the solution is kept under dark conditions for 30 min, so that the adsorption-desorption equilibrium is achieved between the RhB dye and photocatalyst KNN. The sample is irradiated by the visible light. At fixed time intervals of 30 min within 3 h, 4 mL of suspension is taken out and centrifuged at 8000 rpm for 10 min in order to separate the dye solution from the photocatalyst. The dye degradation process is studied by analysing the visible absorption spectrum.

3 Results and discussion

3.1 Structural and microstructural analysis

The Fig. 2 shows the X-ray diffraction (XRD) patterns of the KNN ceramics prepared with different synthesis methods at room temperature. Both samples are found to crystallize in pure perovskite structure devoid of any impurity phases. The room temperature crystal structure of KNN ceramic is reported to be orthorhombic [39–43]. A clear splitting of (220) and (200) peaks at $2\theta \sim 46°$, in the XRD pattern (see Fig. 2) suggests that the structure is orthorhombic in KNN-S and KNN-H ceramics [41].

The (111) peak in the KNN-H shifts slightly towards higher angles as compared to that in KNN-S (See inset of Fig. 2). The shift ($2\theta \sim 0.0158(1)°$ at (111) peak) may be attributed to the variation in the lattice strain. The generated lattice strain may be attributed to the
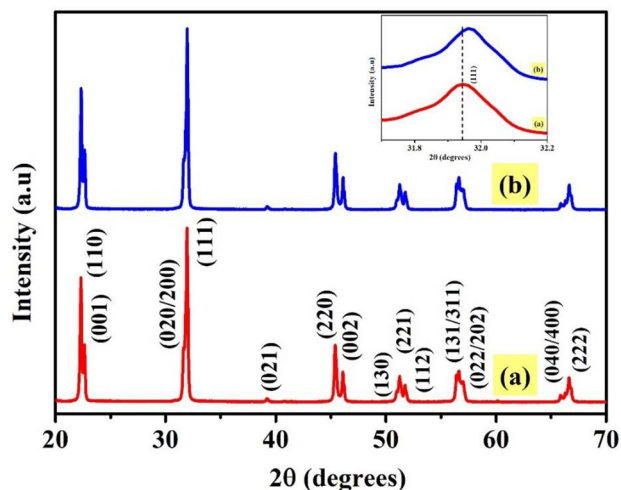
Fig. 2 The XRD pattern of **a** KNN-S and **b** KNN-H ceramics. The orthorhombic pattern is indexed according to JCPDS data file 32–0822 [43]. The inset displays the magnified XRD patterns of the KNN-H and KNN-S ceramics at 2θ ~32°

processing dependent volatilization of K$^+$, Na$^+$ and associated oxygen vacancies [44]. The Table 1 shows the structural parameters obtained by Rietveld refinement, crystallite size and lattice strain for KNN-S and KNN-H samples. The lattice strain is higher in the case of KNN-H as can be seen in Table 1. The crystallite size and lattice strain are determined using the Willamson Hall equation: $\beta\cos\theta = \left(\frac{K\lambda}{D}\right) + 4\varepsilon\sin\theta$ (see supplementary materials) [45] (where, K=0.94). The crystallite size is smaller in KNN-H as compared to that in KNN-S and is consistent with microstructural studies. The Rietveld refinement of the XRD patterns was carried out using FULLPROF(2000) software [46]. In general, the structural models such as *Amm2* (orthorhombic), *Bmm2* (orthorhombic) and *P1m1* (monoclinic) are used in Rietveld refinements of the reported XRD patterns of KNN [40, 41, 47–50]. However, in our study, the *Amm2* (orthorhombic) model (JCPDS data file 32–0822)
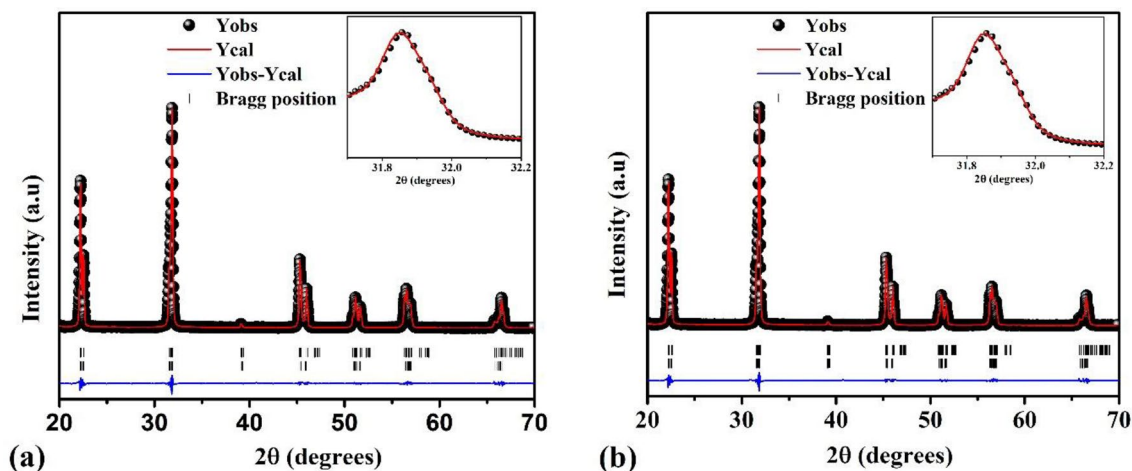

Fig. 3 Rietveld refinement of the XRD patterns of **a** KNN-S and **b** KNN-H ceramics. The fitting of the KNN-H and KNN-S ceramics at 2θ nearly 32° are shown in the inset of the corresponding plots. Solid blue line indicates the deviation between the calculated and observed patterns. Vertical bars at the bottom indicate the 2θ positions of all possible Bragg reflections

Table 1 Structural parameters obtained by Rietveld refinement, crystallite size and lattice strain for KNN-S and KNN-H samples

Sample	KNN-S	KNN-H
Crystal phase	Orthorhombic (*Amm2*)	Orthorhombic (*Amm2*)
Lattice parameters (Å)	$a = 3.9451(3)$	$a = 3.9437(6)$
	$b = 5.6413(5)$	$b = 5.6406(3)$
	$c = 5.6729(1)$	$c = 5.6721(5)$
	$\alpha = \beta = \gamma = 90°$	$\alpha = \beta = \gamma = 90°$
Cell volume (Å^3)	126.2542(4)	126.1758(7)
Refinement quality	$\chi^2 = 3.38, R_p = 6.27, R_{wp} = 7.42g$	$\chi^2 = 3.74, R_p = 6.67, R_{wp} = 7.81$
Crystallite size (nm)	64 ± 3	39 ± 2
Lattice strain	0.00115 ± 0.00009	0.00191 ± 0.00013

is found to be most appropriate [43]. The Fig. 3 shows Rietveld refinement of the XRD patterns of the KNN ceramics prepared with different synthesis methods. The obtained lattice parameters and refinement quality factors for both KNN ceramics are listed in the Table 1. The lattice parameters and atomic positions (see supplementary materials) are consistent with those reported in earlier studies [41, 51].

The microstructures of KNN-S and KNN-H are displayed in Fig. 4a and b, respectively. KNN-H ceramic has the apparent density, $\rho_a = 4.24$ g/cm^3 and relative density $\rho_r = 94\%$. In comparison to the KNN-H ceramic, the microstructure of the KNN-S ceramic is denser with apparent density, $\rho_a = 4.36$ g/cm^3 and relative density, $\rho_r = 96\%$. As expected, the observed density is smaller than the theoretical density of 4.51 g/cm^3 [52]. The grain size is computed using the linear intercept approach as implemented in ImageJ software [53]. The Gaussian distribution is fitted to estimate the average grain size of KNN-S and KNN-H samples, as shown in Fig. 4c and d, respectively. The average grain size is found to be $2.07 \pm 0.05 \mu m$ and $0.89 \pm 0.03 \mu m$ for KNN-S and KNN-H ceramics, respectively. A higher percentage of grain boundaries are seen in KNN-H than that in KNN-S due to lower rate of diffusion in KNN-H which in turn is due to its lower calcination temperature.

3.2 Dielectric properties

The Fig. 5 shows the temperature dependence of the relative dielectric permittivity and dielectric loss (tanδ) at different frequencies revealing the phase transition behaviour and electrical characteristics of KNN ceramics. The two permittivity peaks (See Fig. 5) indicate the phase transition of KNN above room temperature. The phase transition from tetragonal to cubic phase (T_{T-C}) is represented by the higher temperature peak, while the orthorhombic to tetragonal phase transition (T_{O-T}) is represented by the lower temperature peak [31, 54, 55]. The magnitudes of T_{O-T} and T_{T-C} for KNN-S ceramic are found to be ~ 204 and ~ 420 °C,
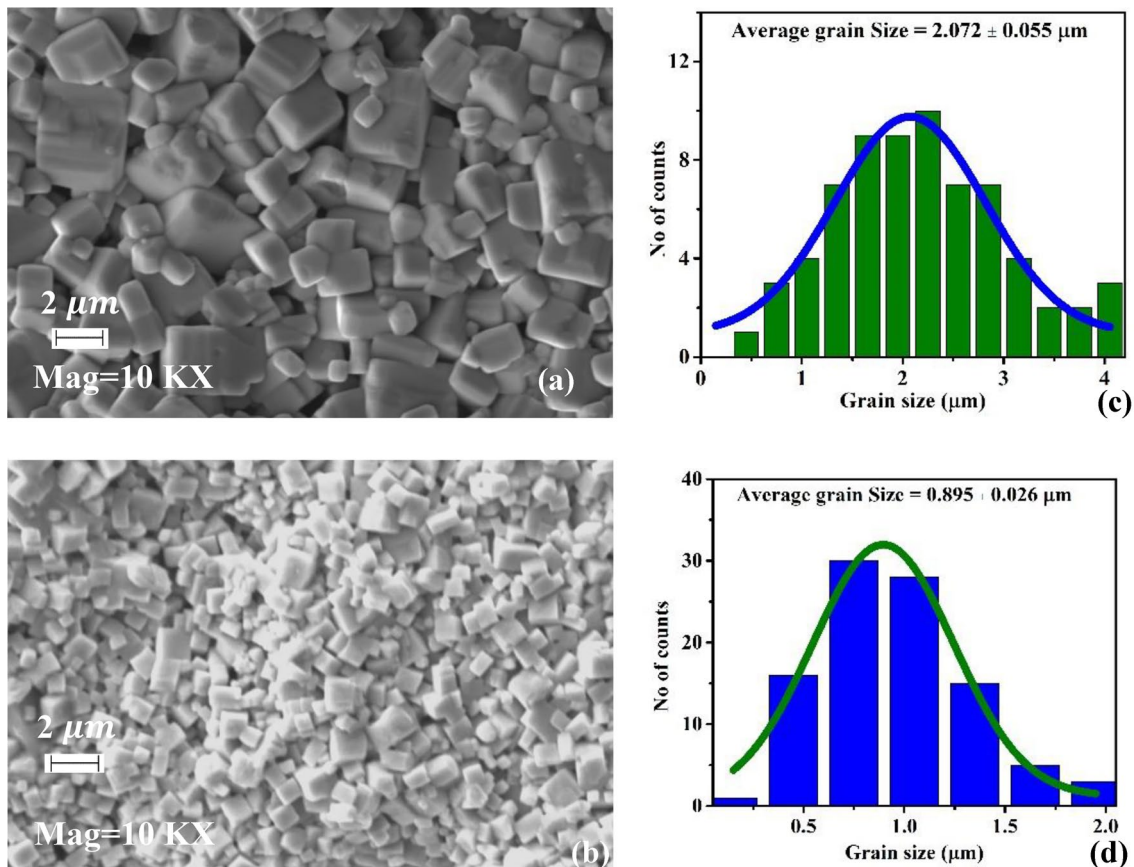

Fig. 4 SEM images of sintered samples of **a** KNN-S and **b** KNN-H ceramics. The distribution of the grain size of **c** KNN-S and **d** KNN-H ceramics
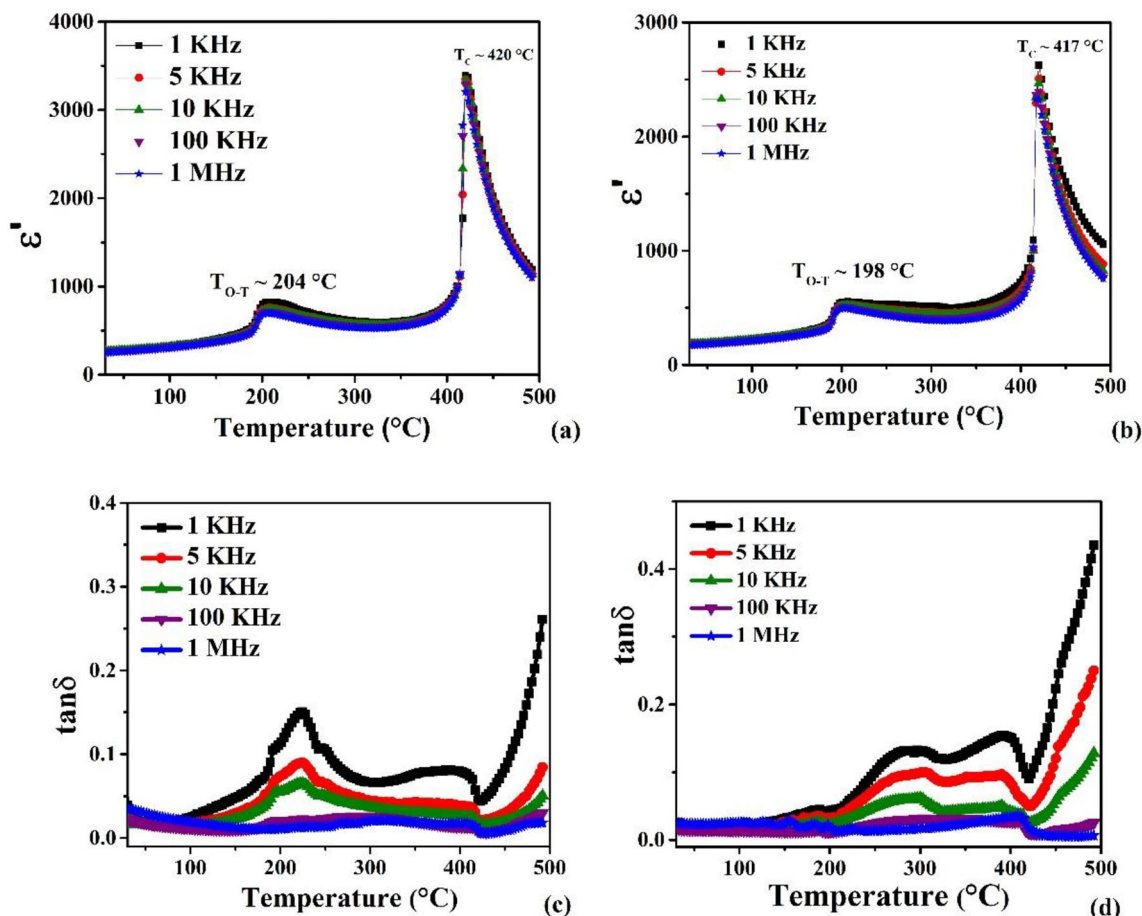
Fig. 5 Temperature dependent relative dielectric permittivity (ϵ') of **a** KNN-S and **b** KNN-H ceramics at different frequencies. Temperature dependent dielectric loss (tanδ) is plotted for **c** KNN-S and **d** KNN-H ceramics at different frequencies

respectively (Fig. 5a). The T_{O-T} and T_{T-C} values in case of KNN-H ceramic are − 198 and − 417 °C, respectively (Fig. 5b). The KNN-S ceramic is found to have greater relative dielectric permittivity and lower dielectric loss (Fig. 5c and d) than those in KNN-H ceramic. For KNN-H ceramic, the number of grain boundaries rises due to smaller grain size. This results in the possibility of space charges accumulation across the grain boundaries. As a result, KNN-H ceramic has a lower relative dielectric permittivity value than KNN-S ceramic.

The Curie-Weiss law describes the dielectric permittivity of conventional ferroelectric systems in the paraelectric region above the Curie point. The Curie-Weiss law is given as $\epsilon' = \frac{C}{T-T_{cw}}$, where C is Curie-Weiss constant and T_{cw} is Curie-Weiss temperature [56, 57]. The behaviour of the dielectric permittivity near T_{cw} is studied by plotting the inverse dielectric permittivity as a function of temperature at 100 kHz frequency as illustrated in Fig. 6a and b. The linear

nature of the inverse dielectric permittivity at T > T_{cw} indicates that both the KNN ceramics obey the Curie-Weiss law. There is no significant mismatch in ionic radii (IR) and charge between the K$^+$ (IR = 1.64 Å, CN = 12) and Na$^+$ (IR = 1.39 Å, CN = 12) [58] and therefore no sizeable disorder in the systems. Based on this the PNR (polar nano region) theory suggests that pure KNN cannot display relaxor behaviour. In general, the dielectric permittivity for diffusive structural phase transition deviates from the Curie-Weiss law in the temperature range $T_{cw} < T < T_B$, where T_B is the Burn temperature at which the linearity starts to deviate. T_B is also the maximum temperature at which local polarisation begins [59]. Here the deviation, $\Delta T_{max} = T_B - T_{max} \approx 0$ (because of $T_B \approx T_{max}$) for the both KNN-S and KNN-H ceramics; where T_{max} is the temperature which exhibit maximum relative dielectric permittivity. The obtained values of different temperatures and other parameters of the samples are
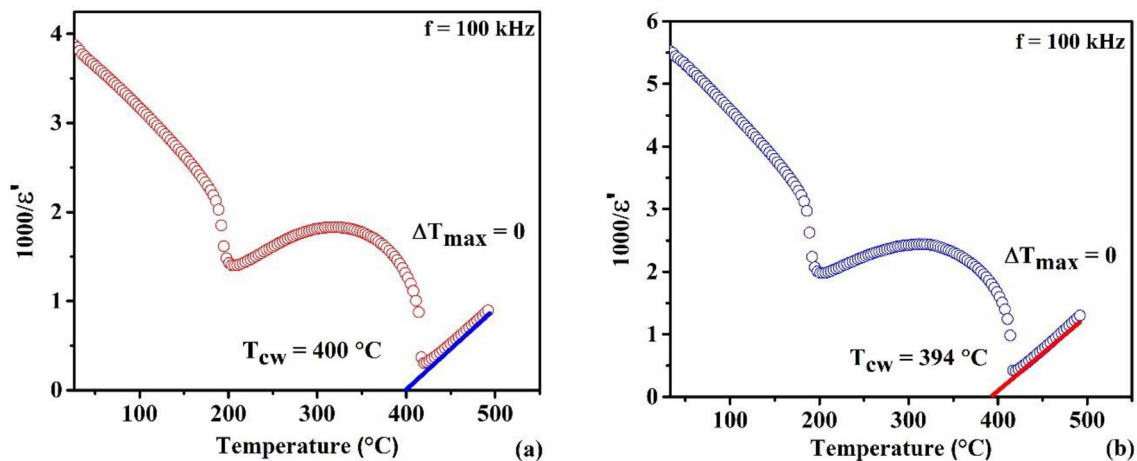
Fig. 6 Variation of inverse dielectric permittivity with temperature for **a** KNN-S and **b** KNN-H ceramics at 100 kHz frequency

listed in Table 2. The modified Curie-Weiss law [60] is given as:

$$\frac{1}{\epsilon'} - \frac{1}{\epsilon'_{max}} = \frac{(T - T_{max})^{\gamma}}{C} \tag{1}$$

where C is the Curie constant and γ is the diffusion coefficient. A normal ferroelectric system is represented by $\gamma = 1$ and an ideal relaxor ferroelectric system by $\gamma = 2$. The magnitude of γ is found to be 1.18 ± 0.01 and 1.12 ± 0.01 for KNN-S and KNN-H ceramics (see supplementary materials), indicating predominantly normal ferroelectric nature or the presence of only the minor degree of relaxor behaviour. This is also consistent with PNR (polar-nano-regions) theory that suggests the absence of relaxor behaviour

in KNN due to comparable ionic radii and charges of K^+ and Na^+. However, nominal dispersion has been observed in KNN-H between 200 and 400 °C which is insignificant in case of KNN-S.

3.3 Ferroelectric properties

The Fig. 7 shows the hysteresis curves of polarization (P) and current (I) as a function of electric field (E) for the KNN ceramics. The measurements are performed at the room temperature with an applied frequency of 1 Hz till electrical breakdown occurs. In general, the leakage current and switching current caused by domain switching mechanisms are the two forms of current signals that are seen when ferroelectric materials are subjected to external electric fields. The

Table 2 The average grain size, dielectric permittivity, phase transition temperatures, and diffusion coefficient according to modified Curie-Weiss law at 100 kHz of KNN-S and KNN-H ceramics. Comparative values with respect to reported systems are also given

KNN system	Average grain size(μm)	ϵ'_{max}(at 100 kHz)	ϵ' at room temperature	T_{o-T}(°C)	$T_c = T_{max}$(°C)	T_{cw}(°C)	T_B(°C)	γ
KNN-S (This work)	2.07 ± 0.05	3286	315	204	420	400	420	1.18 ± 0.01
KNN-H (This work)	0.89 ± 0.03	2394	227	198	417	394	417	1.12 ± 0.01
Ref. [59]	–	4500*	450*	200	403	379	403	1.19
Ref. [61]	–	5000*	310	202	429	–	–	1.12
Ref. [62]	5.20	4000*	420*	200*	428	–	–	1.03
Ref. [41]	1.06	3200*	250	190	406	–	–	–
Ref. [63]	2.00	2400*	300*	206	408	–	–	–
Ref. [38]	3.90	5000*	338	200	420	–	–	–
Ref. [7]	–	8430*	648	200*	372	–	–	1.25

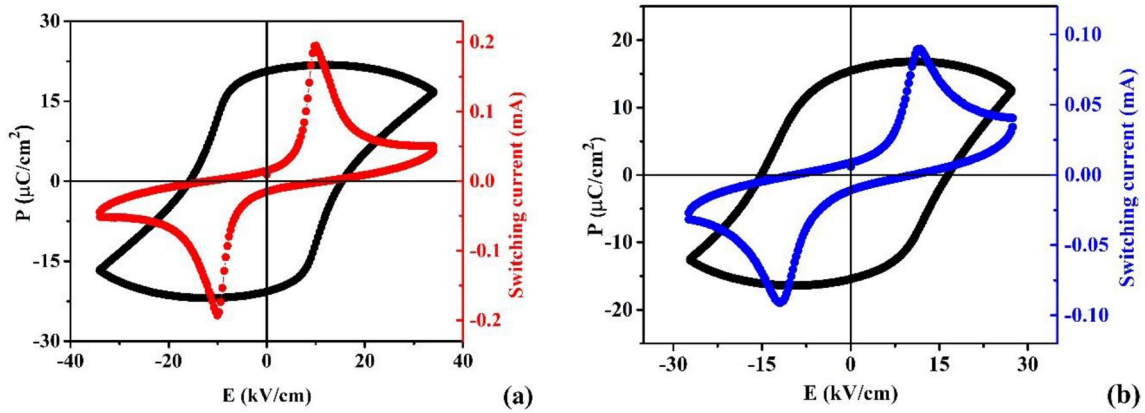*Denotes approximated values based on the plots presented in the references

Fig. 7 Room temperature *P–E* and *I–E* loops measured at 1 Hz frequency for **a** KNN-S and **b** KNN-H ceramics

ferroelectric nature of KNN ceramics is confirmed by the presence of a domain switching current peak (Fig. 7) when an electric field is applied. As the applied electric field is increased, the amplitude of the domain switching current peak grows until it is eventually saturated for both KNN ceramics and the corresponding P–E loops exhibit the symmetrical curves. The peak in the current signal at the electric field less than the maximum value, indicates the occurrence of domain switching. The applied electric field corresponds to the current peak in the I–E curve denotes the coercive field (E_c). The KNN-H ceramic shows lower polarisation (i.e., P_r and P_{max}) and a slightly higher E_c than the KNN-S ceramic (Table 3). Because of small grain size more grain boundaries are present in the KNN-H ceramic as compared to KNN-S ceramic. The Fig. 8 shows a schematic diagram of the energy barriers with respect to the grain sizes for both ceramics. The ferroelectric domains are switched when the energy barrier

is overcome. In general, the energy barrier decreases with increasing grain size. As a result, reversal of the polarisation of a ferroelectric domain inside a smaller grain is much difficult than that in the larger grain [64].

Hence, domain switching, and domain wall motion are comparatively difficult in the KNN-H ceramic because of the clamping effect from the surrounding grains. It has been found that smaller grains possess less crystallinity and are more difficult to switch in polarity, as compared to the large grains [65].

There are two aspects to the impact of the grain boundaries on polarisation. The grain boundary is a low-permittivity area. Thus, ferroelectric ordering is poor at the grain boundary. Consequently, the polarisation at the grain boundary may be absent or minimal. On the other hand, depletion layer can form on the grain surface when space charges in the grain boundary exclude polarisation charges on the grain
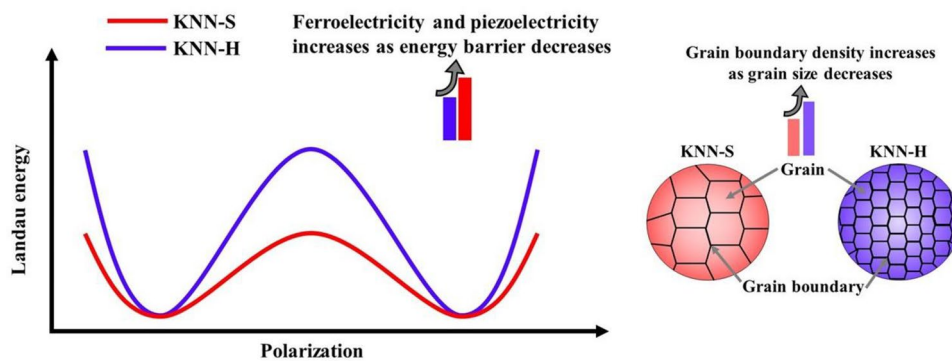

Fig. 8 Schematic of the energy barriers with respect to the grain sizes for both ceramics. The vertical bars on the left side are used for comparison of ferroelectric and piezoelectric property, whereas the vertical bars on the right side are used for comparison of grain boundary density of KNN-S and KNN-H ceramics

Table 3 Variation of P_r, P_{max}, and E_c values with different grain size obtained from hysteresis loops of KNN ceramics

KNN system	Average grain size (µm)	P_r(µC/cm^2)	E_c (kV/cm)	P_{max}(µC/cm^2)
KNN-S (This work)	2.07 ± 0.05	20.41	15.17	22.45
KNN-H (This work)	0.89 ± 0.03	15.38	16.24	17.43
Ref. [63]	2.00	16.00*	17.00*	18.00*
Ref. [9]	1.16	16.42	11.52	20.00*
Ref. [38]	3.90	11.40	8.50	15.00*
Ref. [61]	–	20.00*	22.00*	25.00*
Ref. [62]	5.20	25.00*	15.00*	30.00*
Ref. [7]	–	9.84	10.93	15.00*

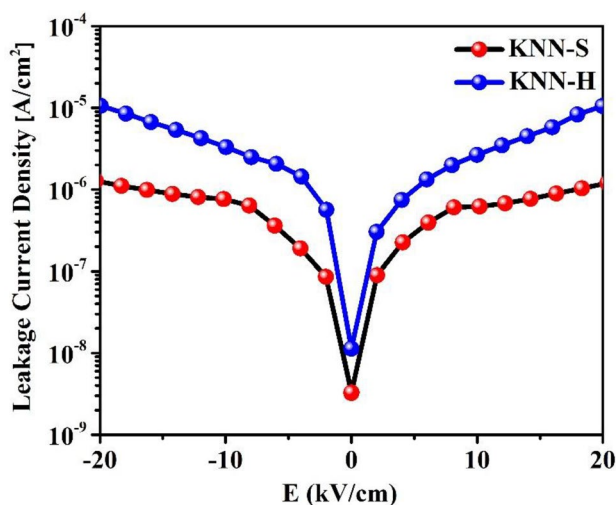*Denotes approximated values based on the plots presented in the references

Fig. 9 Leakage current density versus electric field plots of KNN-S and KNN-H ceramics at room temperature

surface. As a result, there is a polarisation discontinuity on grain surface, which creates a depolarization field and polarization decreases [64]. This results in the reduction in P_r and P_{max} for KNN-H ceramic. The variation in grain size (t) influences the domain size (d), which in turn significantly influences the ferroelectric characteristics. The domain size is directly correlated with grain sizes well above 100 nm as $d \propto t^{\frac{1}{2}}$ [66].

The Fig. 9 shows the room temperature leakage current as function of electric field varying from − 20 kV/cm to + 20 kV/cm. For both KNN-S and KNN-H samples, the leakage current density increases significantly with increasing electric field due to formations of defect states and K/Na ions vacancies. The evaporation of K/Na ions results in formation of oxygen vacancies that in turn increases the leakage current at higher applied electric fields [67]. The leakage current density

in KNN-S is less in comparison to that in KNN-H ceramic at all electric fields. The leakage current densities of KNN-S and KNN-H, at electric field of 20 kV/cm, are found to be 1.2×10^{-6} A/cm^2 and 10.5×10^{-6} A/cm^2, respectively. The reduction in leakage current in the KNN-S ceramic suggests the enhancement of insulating nature which is associated with reduction of oxygen vacancies. We further perform the impedance spectroscopic measurements and discuss them in Sect. 3.4, in order to understand the microscopic mechanisms that may improve the leakage current density of KNN-S ceramic.

3.4 Impedance spectroscopy analysis

Next, we study the dielectric relaxation phenomena by analysing the impedance data for KNN in the temperature range from 430 to 500 °C.

The Cole-Cole plots of KNN ceramics in the frequency range (20 Hz – 1 MHz) and above Curie temperature are shown in the Fig. 10. The temperature variation of bulk resistivity (ρ_b) due to the grains is plotted for KNN-S and KNN-H ceramics and shown in Fig. 11. The temperature dependent resistivity of KNN-S ceramic is found to be higher than that for KNN-H ceramic. Figure 10 shows the nonlinear (semicircle) nature of Z'' (where $Z^* = Z' - jZ''$) and increases with temperature above 430 °C. This indicates the decrease in insulating behaviour in the sample at higher temperatures. The observed single semi-circular arc is indicative of the electrical properties arising primarily due to the bulk effects. Further, the intercept point on the real axis shifts towards the origin as the temperature increases, indicating the decrease in the resistivity. The bulk resistance R_b is estimated using an equivalent circuit that consists bulk resistance R_b
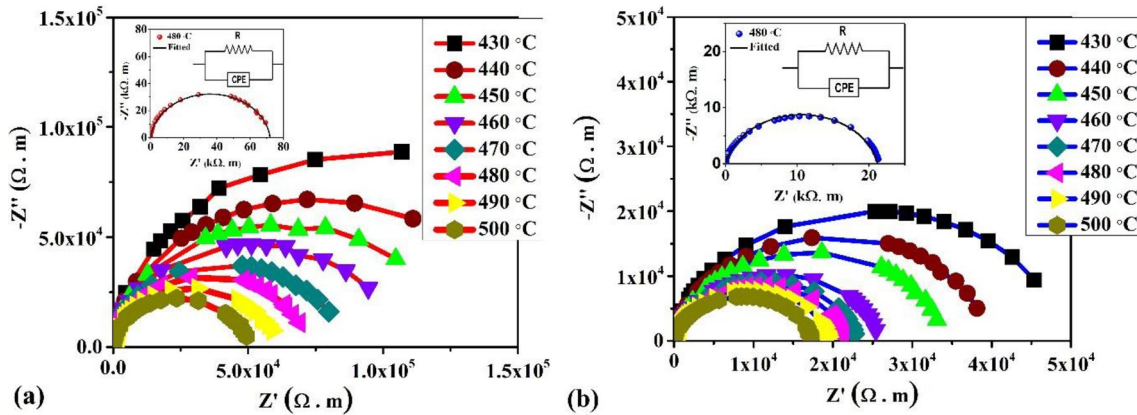
Fig. 10 The real and imaginary part of impedance at different temperatures for **a** KNN-S and **b** KNN-H ceramics. The insets of (a, b) show the proposed electrical equivalent circuit
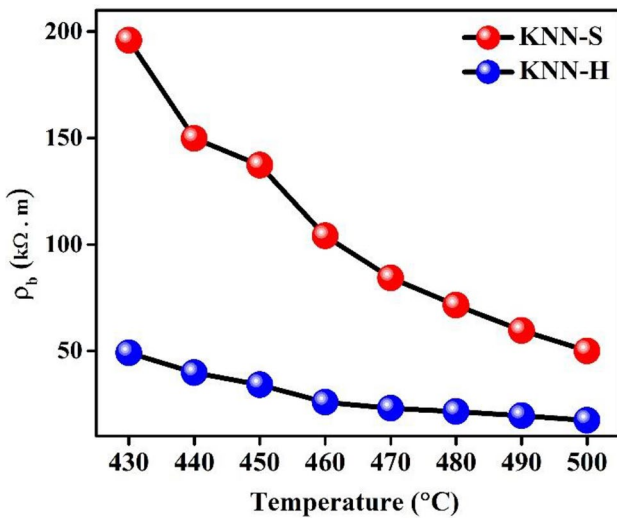

Fig. 11 The bulk (grain) resistivity (ρ_b) as function of temperature for KNN-S and KNN-H ceramics

and bulk capacitance C_b in parallel combination. Using this model, the real Z′ (ω) and imaginary Z″(ω) components of complex impedance ($Z^* = Z' - jZ''$) can be expressed as [68, 69]:

$$Z' = \frac{R_b}{(1 + \omega C_b R_b)^2} \tag{2}$$

$$Z'' = \frac{\omega C_b R_b^2}{(1 + \omega C_b R_b)^2} \tag{3}$$

The impedance data with non-ideal behaviour are fitted using an equivalent circuit with one R and one

CPE or constant phase element (Q) as shown in Fig. 10 [69, 70]. The capacitance (C), resistance (R) and Q are related as [71] :

$$C = (R^{1-n} \times Q)^{1/n} \tag{4}$$

Where, $C = C_b$ and $R = R_b$

The CPE admittance is given as [72]:

$$Y(CPE) = Y_0 \omega^n \left\{ \cos\left(\frac{n\pi}{2}\right) + j\sin\left(\frac{n\pi}{2}\right) \right\} \tag{5}$$

The Table 4 shows the magnitudes of R as well as n which is an empirical constant representing the deviation from an ideal Debye behaviour. The n varies between 0 and 1 with 0 for the ideal resistor and 1 for the ideal capacitor.

The Fig. 12 shows the imaginary part of the electric modulus (M'') as function of frequency. As can be seen, for the given temperature, the M'' increases with increasing frequency and attains maximum for both samples. Further, the maximum value of M'' increases and its peak position shifts towards high frequency as the temperature increases. This behaviour indicates the relaxation behaviour that is dependent on the temperature. The frequency at the M'' peak (f_{max}), the activation energy (E_a) for the electrical response and the temperature (T) are related via the Arrhenius relationship as:

$$f_{max} = f_0 \exp(-E_a/k_B T)$$

$$\ln(f_{max}) = \ln(f_0) - \frac{E_a}{k_B T} \tag{6}$$

Table 4 The parameter n, bulk resistance and bulk capacitance for KNN-S and KNN-H ceramics at different temperatures extracted by Cole-Cole fitting

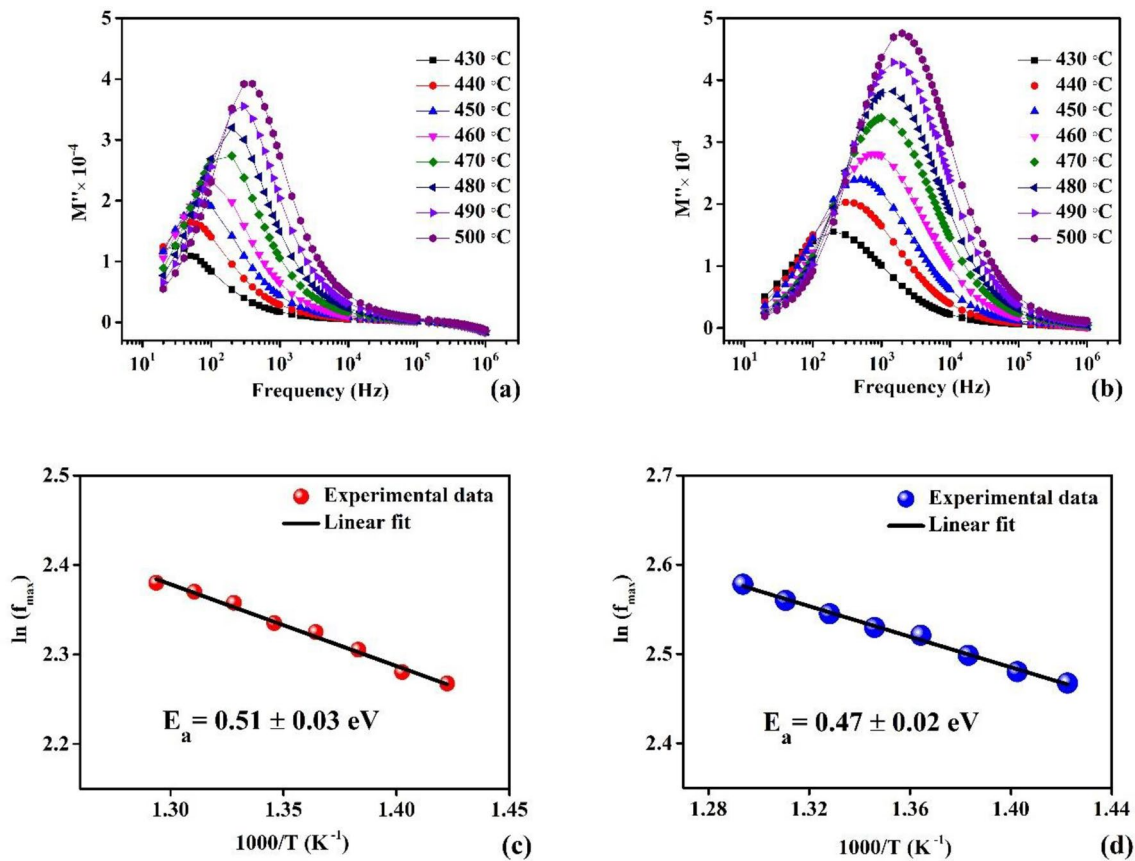| Tempera-ture (°C)	KNN-S				KNN-H			
	n	ρ_b (kΩ.m)	R_b (kΩ) $\times 10^3$	C_b (F) $\times 10^{-8}$	n	ρ_b (kΩ.m)	R_b (kΩ) $\times 10^3$	C_b (F) $\times 10^{-8}$
430	0.940	195.97	5.58	4.42	0.879	49.12	1.19	4.76
440	0.932	149.85	4.27	3.53	0.878	39.75	0.969	3.66
450	0.919	137.24	3.91	3.28	0.872	34.11	0.832	3.20
460	0.927	104.02	2.96	2.56	0.862	25.91	0.632	2.92
470	0.932	84.28	2.39	2.06	0.863	23.07	0.562	2.42
480	0.933	71.47	2.03	1.79	0.862	21.54	0.525	2.14
490	0.938	59.62	1.69	1.59	0.862	19.56	0.476	1.93
500	0.928	49.99	1.42	1.51	0.861	17.38	0.423	1.75

Fig. 12 The variation of the imaginary part of the electric modulus (M″) with frequency at different temperatures for **a** KNN-S and **b** KNN-H ceramics. The corresponding Arrhenius plots for **c** KNN-S and **d** KNN-H ceramics

Where, k_B is the Boltzmann's constant and f_0 is pre-exponential factor.

Figure 12c and d show the plots of $\ln(f_{max})$ as function of $1/T$ for the KNN-S and KNN-H ceramics, respectively. The E_a magnitudes for the KNN-S and KNN-H ceramics are found to be 0.51 ± 0.03 and 0.47 ± 0.02 eV, respectively. The E_a values for both KNN-S and KNN-H ceramics are near to the reported value [73]. The slightly lower activation energy for KNN-H ceramic, may be attributed to the increased

hopping of the charge carriers between the neighbouring lattice sites [74].

In KNN ceramics, the Na/K cation vacancies are generated due to their volatile nature at high temperatures (> 800 °C). This in turn results in creation of oxygen vacancies. The single and doubly ionized oxygen vacancies have been reported to have activation energies in the range ~ 0.3–0.5 eV and ~ 0.6–1.2 eV, respectively [70]. The obtained E_a values suggest that the single-ionized oxygen vacancies are primarily formed in KNN-S and KNN-H ceramics due to formation of K⁺/Na⁺ vacancies during the phase formation of the ceramics. The Kröger-Vink notation for this process is given as [70, 75]:

$$Na_{Na} \rightarrow Na + V'_{Na} + h^{\bullet} \tag{7}$$

$$K_K \rightarrow K + V'_K + h^{\bullet} \tag{8}$$

$$O_O \rightarrow \frac{1}{2}(O_2) + V_O^{\bullet} + e' \tag{9}$$

Where V'_{Na} and V'_K are the concentration of the sodium and potassium vacancies. The resistance R_b decreases with increasing temperature indicating the negative temperature coefficient of resistance (NTCR) behaviour [69]. The KNN-S ceramic shows the enhanced grain resistance as compared to that for KNN-H ceramic due to the enhancement of the grain growth. The grain growth occurs due to increased diffusion rate and mass transfer through grain boundaries at higher sintering temperatures [76].

3.5 Piezoelectric properties

Next, we discuss the piezoelectric properties of KNN-S and KNN-H ceramics. The Fig. 13 shows piezoelectric coefficient (d_{33}) of these ceramics as a function of poling electric field at room temperature. The KNN ceramics are poled in silicon oil at the room temperature and by applying DC electric field. The applied maximum DC electric field is kept at 35 kV/cm for 40 min on the sintered pellets. The d_{33} is found to be almost constant for electric field between 25 and 35 kV/cm. The dielectric breakdown in both the samples occur above 35 kV/cm. However, at higher poling fields, the contribution from the 180° domain switching is found to be significantly lower than that from non 180° domain switching. This results in enhancement of d_{33} values as material undergoes deformation at
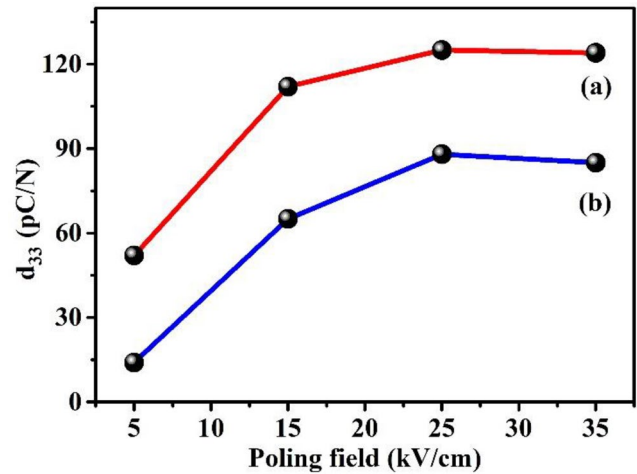

Fig. 13 Piezoelectric coefficient (d_{33}) of **a** KNN-S and **b** KNN-H ceramics as a function of poling electric field at room temperature

Table 5 Piezoelectric parameters for KNN-S and KNN-H ceramics:

KNN System	d_{33} (pC/N)	k_p
KNN-S (This work)	125	0.28
KNN-H (This work)	88	0.19
Ref. [38]	96	0.28
Ref. [61]	106	0.46
Ref. [41]	60	–
Ref. [63]	85	–
Ref. [7]	71	–
Ref. [21]	110	0.39
Ref. [36]	80	0.36

higher poling fields due to induced strains [77]. The measured d_{33} values for the poled KNN ceramics are shown in Table 5. At every poling field, the d_{33} value obtained for KNN-S ceramic (125 pC/N) is greater than that of KNN-H ceramic (88 pC/N). In general, the piezoelectric coefficient depends on the grain size, relative density, and crystal structure [64]. Since crystal structures of KNN ceramics do not show significant variation, the major factors affecting the d_{33} value should be grain size and relative density. Also, the piezoelectric coefficient is closely correlated with relative dielectric permittivity (ϵ') and remnant polarization (P_r) as: $d_{33} \sim \epsilon' P_r$ [78]. In case of the KNN-H ceramic, an increase in the space charge layer due to large number of grain boundaries would restrict the domain switching under the poling field. Therefore,

the domain wall motion is more restrictive leading to lower d_{33} value than that for KNN-S ceramic. Thus, the higher values of d_{33} obtained for KNN-S ceramic is due to higher relative density and higher $\epsilon' P_r$ value.

The Fig. 14 shows the frequency dependent impedance of poled KNN ceramics at room temperature. The planer electromechanical coupling factor (k_p) is calculated from the measured resonant spectra using equation [79]:

$$k_p^2 = 2.51 \times \frac{f_a - f_r}{f_r} \qquad (10)$$

Where, f_r and f_a are resonance and anti-resonance frequency, respectively. The calculated k_p value of KNN-S and KNN-H ceramics are 0.28 and 0.19, respectively. The decrease in k_p for KNN-H ceramic with smaller grains is likely to be due to fewer domains and less mobile domain walls [80]. The higher k_p and d_{33} values for KNN-S ceramic with larger grains indicate the enhancement of piezoelectric properties as compared to those for KNN-H.

3.6 Ultraviolet–visible (UV–Vis) diffuse reflectance spectra

The UV–Vis diffuse reflectance spectra $F(R)$ are measured and the Tauc plots are obtained using equation as [81]:

$$[F(R)h\nu]^n = A\left(E_g - h\nu\right) \qquad (11)$$

Where $F(R)$, E_g and ν are Kubelka–Munk function, bandgap and light frequency, respectively.

$F(R)$ is the Kubelka–Munk function and it can be determined by the following equation-

$$F(R) = (1 - R)^2 / 2R \qquad (12)$$

Where, R is the relative reflectance. The parameter n is 2, if the band gap is direct, while n equals 0.5 for the indirect band gap. The bandgap for the KNN-based materials has been reported to be direct with $n = 2$ [82]. The Fig. 15 shows the room temperature UV–Vis diffuse reflectance spectra and the Tauc plots for KNN ceramics. From these plots, the bandgap (E_g) values are estimated to be 3.48 and 3.40 eV for the KNN-S and KNN-H ceramics, respectively. The estimated bandgap values are in agreement with the earlier reported values [29, 83]. The Fig. 15, also shows a slightly higher tail structure near the bottom of the absorption edge for KNN-H as compared to the KNN-S ceramic. This suggests the presence of higher defect concentration
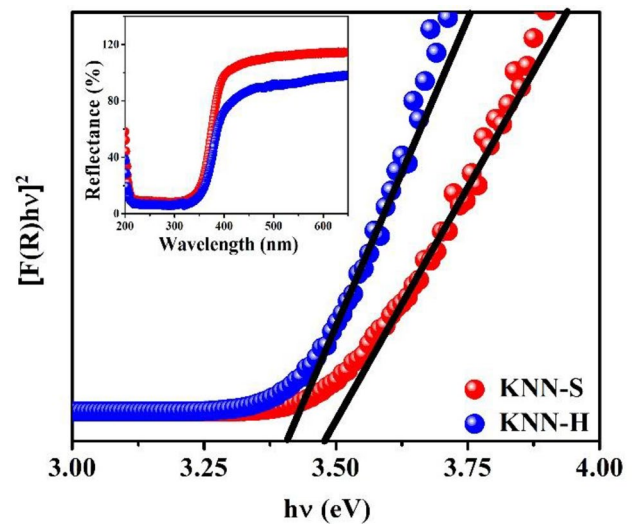

Fig. 15 Tauc plots and UV–Vis diffuse reflectance spectra (shown in inset) for KNN-S and KNN-H ceramics
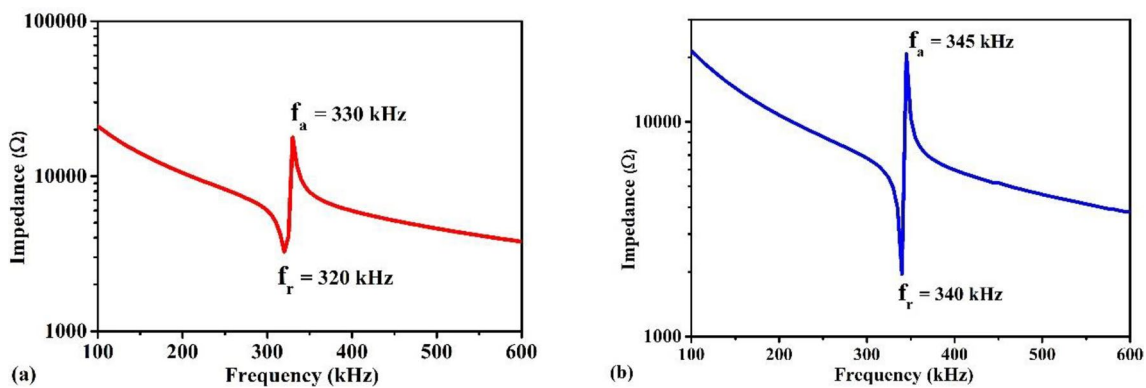

Fig. 14 Impedance as function of frequency for **a** KNN-S and **b** KNN-H poled ceramics at room temperature

in KNN-H sample compared to that in KNN-S sample [84, 85]. These defect states also result in slightly lower value of optical band gap energy of KNN-H ceramic [67]. Because of higher band gap value of KNN-S ceramic than KNN-H ceramic, insulating property will be higher in KNN-S ceramic, which is also reflected in impedance data and leakage current measurement.

3.7 Photocatalytic properties of KNN

Ferroelectric materials are particularly interesting and promising as photocatalysts due to presence of spontaneous polarization in them. The separation of photogenerated charges in photocatalysis mainly relies on the internal electric field. In ferroelectrics, the internal electric field can be usually quite strong due to spontaneous electric polarization. The Fig. 16 shows the schematic of photocatalytic activity in ferroelectric materials. As can be seen, the electrons and holes are accumulated at the C^+ and C^- surfaces, respectively. This leads to surface band bending which in turn promotes the charge carrier transport to absorbed intermediates (hydroxyl radicals and atomic hydrogen).

As the KNN particles is irradiated by visible light, the photo-induced electrons react with oxygen molecules (O_2) at the catalyst surface and produce superoxide radical ($\bullet\, O_2^-$). On the other hand, the photo-induced holes react with water molecules (H_2O) at the catalyst surface and produce hydroxyl radicals ($\bullet\, OH$). Both these radicals act as major active species during the photocatalytic reaction [86]. The photocatalytic process can be understood by following equations:
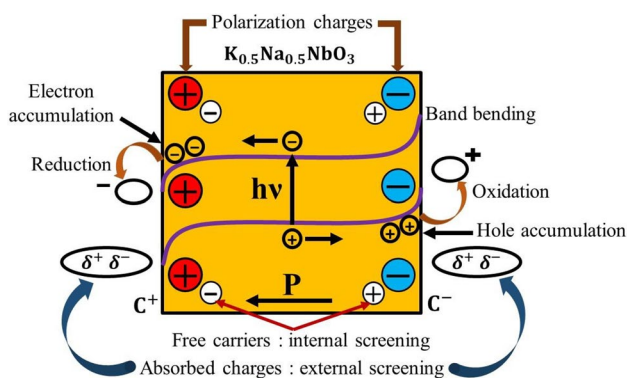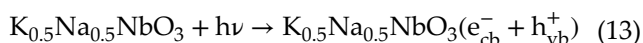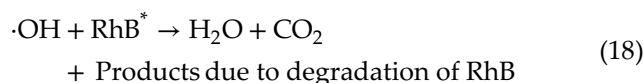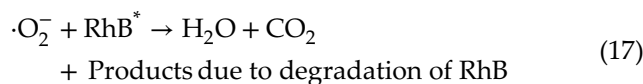
$$K_{0.5}Na_{0.5}NbO_3 + h\nu \rightarrow K_{0.5}Na_{0.5}NbO_3(e_{cb}^- + h_{vb}^+) \quad (13)$$

Fig. 16 Schematic of photocatalytic activity for ferroelectric materials

$$RhB + h\nu \rightarrow RhB^* \tag{14}$$

$$h_{vb}^+ + H_2O \rightarrow\ \cdot OH + H^+ \tag{15}$$

$$e_{cb}^- + O_2 \rightarrow\ \cdot O_2^- \tag{16}$$

$$\cdot O_2^- + RhB^* \rightarrow H_2O + CO_2$$
$$+ \text{Products due to degradation of RhB} \tag{17}$$

$$\cdot OH + RhB^* \rightarrow H_2O + CO_2$$
$$+ \text{Products due to degradation of RhB} \tag{18}$$

The Fig. 17 shows the results of photocatalytic activity of unpoled KNN-S and KNN-H in the degradation of the RhB dye solution. The absorbance spectrum exhibits the maximum at $\lambda_{max} = 553$ nm which is the characteristic of the RhB dye solution [11, 87]. The decreasing absorbance of the RhB dye solution with time suggests the gradual decomposition of RhB molecules with time. The Fig. 17 also suggests that the grain size in KNN-S and KNN-H influences the degradation of RhB solution.

Figure 18 shows the change in relative concentration (C/C_0) of the RhB solution as time increases. As can be seen, the KNN-H degrades the dye solution with degradation efficiency of 65% which is higher than the KNN-S degradation efficiency of 20%. The control RhB degradation experiment performed with or without catalyst under dark, light experiments indicated that the decrease in RhB concentration is indeed driven only in the presence of catalyst and light. It has been suggested that the volume recombination of the charge carriers is the dominant process in ferroelectric particles, and can be reduced by decreasing the particle size [88]. As the particles size decreases, the surface-to-volume ratio increase, that in turn, increases the available surface-active sites [89]. The surface area is measured using the BET analyzer and is found to be 4.18 m^2/g for KNN-S and 8.24 m^2/g for KNN-H. We explore the rate kinetics of the photocatalytic reaction of RhB solution, we plot $-\ln\frac{C}{C_0}$ as function of time (t) in Fig. 18b. The linear fit shows that the degradation process of RhB solution can be described by the following pseudo-first-order model [88, 90]:

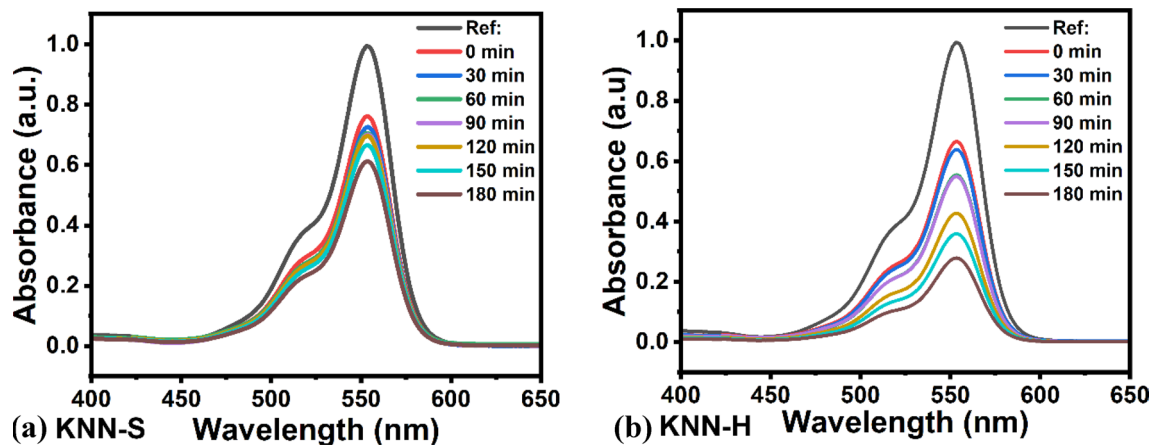$$-\frac{dC}{dt} = kC \ \text{ or } \ -\ln\frac{C}{C_0} = kt \tag{19}$$

Fig. 17 Visible light absorbance spectra of RhB dye solution with **a** KNN-S and **b** KNN-H samples
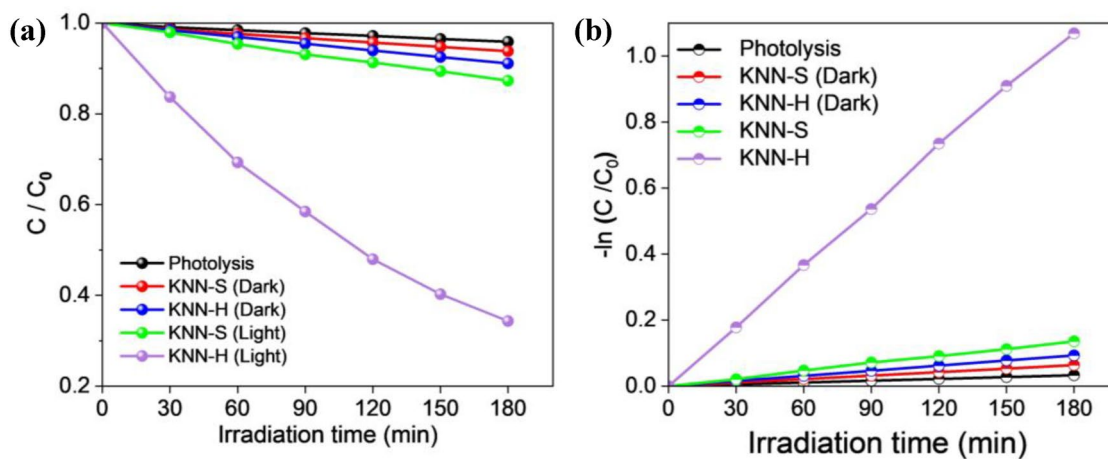

Fig. 18 a C/C_0 vs. time plot (First order kinetics) for RhB dye solution and **b** Plots for rate constant (k) of KNN-S and KNN-H samples

Table 6 Degradation percentage of RhB dye solution and the rate constant (k) for KNN-S and KNN-H ceramics

Samples	Degradation (%)	k values(min^{-1})	Surface area (m^2/g)
KNN-S	20	0.0007	4.18
KNN-H	65	0.0060	8.24

Where k and C are the reaction rate constant, and concentration of dye molecules at time t, respectively. C_0 is the concentration at time $t = 0$. The Table 6 shows the estimated rate constant (k) and the degradation percentage (η) at time $t = 180$ min. As can be seen, the dye degradation efficiency is significantly higher for KNN-H as compared to that for KNN-S.

4 Conclusions

In the present study, the microstructure, dielectric, ferroelectric, and piezoelectric properties of the KNN ceramics synthesized via solid-state reaction (KNN-S) and hydrothermal reaction (KNN-H) are investigated. From the Rietveld refinement of the XRD, the KNN samples at the room temperature are found to have the orthorhombic *Amm2* space group symmetry. The KNN-S ceramics is found to have larger grains and a higher relative density as compared to that for KNN-H. The ϵ', P_r, d_{33} and k_p values are found to be

lower for KNN-H than those for KNN-S possibly due to clamping effect arising from large fraction of grain boundaries. In comparison to KNN-H ceramic, KNN-S has a lower leakage current density value at all electric fields due to reduction of oxygen vacancies. The measured activation energy values indicate that single-ionized oxygen vacancies are primarily generated in KNN-S and KNN-H ceramics during the phase formation of the ceramics. Compared to KNN-H ceramic, the KNN-S ceramic exhibits greater grain resistance due to the enhancement of the grain growth. The negative temperature coefficient of resistance (NTCR) behaviour was also confirmed through impedance study. Impedance and leakage current measurements suggest higher insulating behaviour for KNN-S ceramic as compared to that for KNN-H ceramic. Using UV–Vis diffuse reflectance spectra, a marginally higher bandgap is found for KNN-S ceramic as compared to KNN-H ceramic. Photocatalytic activity of KNN powders is investigated for the degradation of RhB dye under visible light irradiation. Smaller particle sizes obtained from hydrothermal method showed enhanced degradation of the dye because of the higher surface area, indicating possibility to utilize for photocatalytic applications. In summary, our study strongly suggests that the electrical and photocatalytic properties of the KNN ceramics are affected by the different synthesis techniques as well as grain size variations and therefore different synthesis methods can be exploited to tailor the dielectric, piezoelectric and photocatalytic properties of KNN.

Author contributions

MS Synthesis, Investigation, Formal analysis, Writing Original draft. SA Conceptualization, Resource, Visualization, Supervision, Writing-review and editing, Project Administrator. MKN Conceptualization, Resource; Visualization, Supervision, Writing-review and editing, Project Administrator. PPC Resource; Visualization, Writing-review and editing. ChS Conceptualization, Resource; Visualization, Writing-review and editing.

Funding

Data availability

The datasets generated and analysed during the current study are available from the corresponding author on reasonable request.

Declarations

Conflict of interest   The authors declare that they have no known competing financial interests or personal relationships that could have appeared to influence the work reported in this paper.

Supplementary Information   The online version contains supplementary material available at https://doi.org/10.1007/s10854-023-11437-z.

References

1. J. Rödel, K.G. Webber, R. Dittmer, W. Jo, M. Kimura, D. Damjanovic, J. Eur. Ceram. Soc. **35**, 1659 (2015). https://doi.org/10.1016/j.jeurceramsoc.2014.12.013
2. Y. Saito, H. Takao, T. Tani, T. Nonoyama, K. Takatori, T. Homma, T. Nagaya, M. Nakamura, Nature. **432**, 2 (2004). https://doi.org/10.1038/nature03028
3. M.D. Maeder, D. Damjanovic, N. Setter, J Electroceram. **13**, 385 (2004)
4. J. Wu, D. Xiao, J. Zhu, Chem. Rev. **115**, 2559 (2015)
5. Y.J. Dai, X.W. Zhang, K.P. Chen, Appl. Phys. Lett. **94**, 3 (2009)
6. J.F. Li, K. Wang, F.Y. Zhu, L.Q. Cheng, F.Z. Yao, J. Am. Ceram. Soc. **96**, 3677 (2013). https://doi.org/10.1111/jace.12715
7. P. Kumar, M. Pattanaik, Sonia, Ceram. Int. **39**, 65 (2013)
8. J. Fuentes, J. Portelles, A. Pérez, M.D. Durruthy-Rodríguez, C. Ostos, O. Raymond, J. Heiras, M.P. Cruz, J.M. Siqueiros, Appl. Phys. A Mater. Sci. Process. **107**, 733 (2012)
9. S. Domingo, D. Nacional, R. Dominicana, J. Adv. Ceram. **9**, 329 (2020)
10. U. Shanker, M. Rani, V. Jassal, Environ. Chem. Lett. **15**, 623 (2017)

11. V.S. Kujur, R. Gaur, V. Gupta, S. Singh, J. Phys. Chem. Solids. **167**, 110751 (2022)

12. D. Gümüş, F. Akbal, Water. Air. Soil Pollut. **216**, 117 (2011)

13. Y. Cui, J. Briscoe, S. Dunn, D. Meier, G. Viola, R. McKinnon, V. Koval, A. Adomkevicius, S. Dunn, H. Yan, D.H. Yoon, L. Ju, X. Tan, X. Mao, Y. Gu, S. Smith, A. Du, Z. Chen, C. Chen, L. Kou, D. Meier, O. Matar, G. Viola, R. McKinnon, V. Koval, A. Adomkevicius, S. Dunn, H. Yan, S. Banerjee, A. Kakekhani, R.B. Wexler, A.M. Rappe, Nat. Commun. **118**, 1 (2021)

14. P. Senthilkumar, D.A. Jency, T. Kavinkumar, D. Dhayanithi, S. Dhanuskodi, M. Umadevi, S. Manivannan, N.V. Giridharan, V. Thiagarajan, M. Sriramkumar, K. Jothivenkatachalam, ACS Sustain. Chem. Eng. **7**, 12032 (2019)

15. S. Zhang, B. Zhang, D. Chen, Z. Guo, M. Ruan, Z. Liu, Nano Energy. **79**, 105485 (2021)

16. M. Stock, S. Dunn, J. Phys. Chem. C **116**, 20854 (2012). https://doi.org/10.1021/jp305217z

17. Z. Zhao, V. Buscaglia, M. Viviani, M.T. Buscaglia, L. Mitoseriu, A. Testino, M. Nygren, M. Johnsson, P. Nanni, Phys. Rev. B - Condens. Matter Mater. Phys. **70**, 1 (2004)

18. G. Cilaveni, K.V. Ashok Kumar, S.S.K. Raavi, C. Subrahmanyam, S. Asthana, J. Alloys Compd. **798**, 540 (2019)

19. L. Curecheriu, S.B. Balmus, M.T. Buscaglia, V. Buscaglia, A. Ianculescu, L. Mitoseriu, J. Am. Ceram. Soc. **95**, 3912 (2012)

20. C.A. Randall, N. Kim, J.P. Kucera, W. Cao, T.R. Shrout, J. Am. Ceram. Soc. **81**, 677 (1998)

21. H. Birol, D. Damjanovic, N. Setter, J. Eur. Ceram. Soc. **26**, 861 (2006)

22. L. EGERTON, D.M. DILLON, J. Am. Ceram. Soc. **42**, 438 (1959)

23. Y. Zhou, J. Yu, M. Guo, M. Zhang, Ferroelectrics. **404**, 69 (2010)

24. N. Zhang, A.M. Glazer, D. Baker, P.A. Thomas, Acta Crystallogr. Sect. A Found. Crystallogr. **63**, s184 (2007)

25. Y. Zhuang, Z. Xu, F. Li, Z. Liao, W. Liu, J. Alloys Compd. **629**, 113 (2015)

26. Hl. CHENG, J. XIAO, P. GAO, Yy. YAN, Sp. GAO, Hl. DU, Trans. Nonferrous Met. Soc. China. **28**, 1801 (2018).https://doi.org/10.1016/S1003-6326(18)64824-1

27. S. Toyama, H. Hayashi, M. Takesue, M. Watanabe, R.L. Smith, J. Supercrit Fluids. **107**, 1 (2016)

28. G. Stavber, B. Malič, M. Kosec, Green. Chem. **13**, 1303 (2011)

29. Y. long Su, X. Chen, Z. de Yu, H. Lian, D. di Zheng, J. Peng, J. Mater. Sci. 52, 2934 (2017)

30. M. Alam, S. Khilari, K. Jai, Shree, D. Das, AIP Conf. Proc. 2265, 0 (2020)

31. E. Buixaderas, V. Bovtun, M. Kempa, M. Savinov, D. Nuzhnyy, F. Kadlec, P. Vaněk, J. Petzelt, M. Eriksson, Z. Shen, J. Appl. Phys. **107**, 014111 (2010)

32. M. Eriksson, H. Yan, G. Viola, H. Ning, D. Gruner, M. Nygren, M.J. Reece, Z. Shen, J. Am. Ceram. Soc. **94**, 3391 (2011)

33. S. Huo, S. Yuan, Z. Tian, C. Wang, Y. Qiu, J. Am. Ceram. Soc. **95**, 1383 (2012)

34. W. Yang, P. Li, S. Wu, F. Li, B. Shen, J. Zhai, Adv. Electron. Mater. **5**, 1 (2019)

35. H. Gu, K. Zhu, X. Pang, B. Shao, J. Qiu, H. Ji, Ceram. Int. **38**, 1807 (2012)

36. R.E. JAEGER, L. EGERTON, J. Am. Ceram. Soc. **45**, 209 (1962)

37. R. Wang, R. Xie, T. Sekiya, Y. Shimojo, Y. Akimune, N. Hirosaki, M. Itoh, Japanese J. Appl. Physics, Part 1 Regul. Pap. Short Notes Rev. Pap. 41, 7119 (2002)

38. X. Vendrell, J.E. García, X. Bril, D.A. Ochoa, L. Mestres, G. Dezanneau, J. Eur. Ceram. Soc. **35**, 125 (2015)

39. Y. Zhen, J.F. Li, J. Am. Ceram. Soc. **89**, 3669 (2006)

40. K. Wang, J.F. Li, Appl. Phys. Lett. **91**, 2005 (2007)

41. S. Dwivedi, T. Pareek, S. Kumar, RSC Adv. **8**, 24286 (2018)

42. T.A. Skidmore, S.J. Milne, J. Mater. Res. **22**, 2265 (2007)

43. P. Bomlai, P. Wichianrat, S. Muensit, S.J. Milne, J. Am. Ceram. Soc. **90**, 1650 (2007)

44. B.P. Zhang, J.F. Li, K. Wang, H. Zhang, J. Am. Ceram. Soc. **89**, 1605 (2006)

45. R. Rani, S. Sharma, M. Quaglio, R. Rai, S. Bianco, D. Pugliese, C.F. Pirri, Mater. Sci. Appl. **08**, 247 (2017)

46. A. Le Bali, Adv. X-ray Anal. **42**, 191 (2000)

47. M. Kosec, B. Malič, A. Benčan, T. Rojac, Piezoelectric Acoust. Mater. Transducer Appl. 81 (2008)

48. X. Wang, X. Lou, W. Geng, Y. Yao, T. Tao, B. Liang, S.G. Lu, J. Appl. Phys. **130**, 1ENG (2021)

49. W. Ge, Y. Ren, J. Zhang, C.P. Devreugd, J. Li, D. Viehland, J. Appl. Phys. **111**, 103503 (2012)

50. H.E. Mgbemere, M. Hinterstein, G.A. Schneider, J. Appl. Crystallogr. **44**, 1080 (2011)

51. B. Tah, S. Goswami, T. Dasgupta, J. Bera, P. Sinha, D. Kundu, S. Sen, A. Sen, Ferroelectrics. **481**, 119 (2015)

52. M. Kosec, D. Kolar, Mater. Res. Bull. **10**, 335 (1975)

53. C. Huang, M.F. Becker, J.W. Keto, D. Kovar, J. Appl. Phys. **102**, 054308 (2007). https://doi.org/10.1063/1.2776163

54. Y. Guo, K.I. Kakimoto, H. Ohsato, Appl. Phys. Lett. **85**, 4121 (2004)

55. M. Eriksson, H. Yan, M. Nygren, M.J. Reece, Z. Shen, J. Mater. Res. **25**, 240 (2010)

56. G.A. Samara, Phys. Rev. **151**, 378 (1966)

57. J.C. Woolley, J. Mech. Phys. Solid. **6**, 83 (1957)

58. B.Y.R.D. Shannon, M.H.N.H. Baur, O.H. Gibbs, M. Eu, V. Cu, (1976)

59. C.W. Cho, M.R. Cha, J.Y. Jang, S.H. Lee, D.J. Kim, S. Park, J.S. Bae, S.D. Bu, S. Lee, J. Huh, Curr. Appl. Phys. **12**, 1266 (2012). https://doi.org/10.1016/j.cap.2012.03.006

60. K. Uchino, S. Nomura, Ferroelectrics. **44**, 55 (1982)

61. D. Lin, K.W. Kwok, H.L.W. Chan, J. Appl. Phys. **106**, 10 (2009)

62. Z. Liu, H. Fan, C. Long, J. Mater. Sci. **49**, 8107 (2014)

63. Z. Pan, J. Chen, L. Fan, J. Zhang, S. Zhang, Y. Huang, L. Liu, L. Fang, X. Xing, J. Am. Ceram. Soc. **98**, 3935 (2015)

64. V.R. Mudinepalli, L. Feng, W.C. Lin, B.S. Murty, J. Adv. Ceram. **4**, 46 (2015)

65. C.C. Leu, C.Y. Chen, C.H. Chien, M.N. Chang, F.Y. Hsu, C.T. Hu, Appl. Phys. Lett. **82**, 3493 (2003)

66. J.P. Praveen, T. Karthik, A.R. James, E. Chandrakala, S. Asthana, D. Das, J. Eur. Ceram. Soc. **35**, 1785 (2015)

67. S. Kumar, M. Shandilya, S. Thakur, N. Thakur, J. Sol-Gel Sci. Technol. **88**, 646 (2018)

68. N. Panda, B.N. Parida, R. Padhee, R.N.P. Choudhary, J. Mater. Sci. Mater. Electron. **26**, 3797 (2015)

69. A. Kumar, T.D. Rao, V.S. Katta, S.S. Kumar, Raavi, S. Asthana, Phys. B Condens. Matter. **639**, 413926 (2022)

70. P. Palei, P. Kumar, J. Adv. Dielectrics. **1**, 351 (2011). https://doi.org/10.1142/S2010135X11000446

71. S.H. Yoon, C.A. Randall, K.H. Hur, J. Am. Ceram. Soc. **92**, 1758 (2009)

72. B.N. Parida, N. Panda, R. Padhee, P.R. Das, R.N.P. Choudhary, J. Mater. Sci. Mater. Electron. **28**, 1824 (2017)

73. Y. Zhai, Y. Feng, J. Du, J. Xue, J. Shen, Y. Lu, T. Lu, P. Fu, W. Li, J. Hao, Z. Xu, J. Mater. Sci. Mater. Electron. **30**, 4352 (2019)

74. D. Triyono, S.N. Fitria, U. Hanifah, RSC Adv. **10**, 18323 (2020)

75. M.W. Barsoum, *Fundamentals of Ceramics*, vol 4 (Institute of Physics, Bristol, UK, 2003)

76. K. Saenkam, P. Jaita, S. Sirisoonthorn, T. Tunkasiri, G. Rujijangul, ScienceAsia. **47**, 34 (2021)

77. K. Uchino, *Ferroelectric Devices*, 2nd edn. (CRC Press, UK, 2009)

78. S.E. Park, T.R. Shrout, IEEE Trans. Ultrason. Ferroelectr. Freq. Control. **44**, 1140 (1997)

79. H. Li, Y. Hao, Z. Lin, X. He, J. Cai, X. Gong, Y. Gu, R. Zhang, H. Cheng, B. Zhang, Solid State Commun. **353**, 114871 (2022)

80. I. Mahmud, M.S. Yoon, S.C. Ur, Appl. Sci. **7**, 7 (2017)

81. A. Sati, V. Mishra, A. Kumar, M.K. Warshi, A. Sagdeo, R. Kumar, P.R. Sagdeo, J. Mater. Sci. Mater. Electron. **30**, 9498 (2019)

82. Z. Liu, H. Fan, Y. Zhao, G. Dong, J. Am. Ceram. Soc. **99**, 146 (2016)

83. Z. Wang, H. Gu, Y. Hu, K. Yang, M. Hu, D. Zhou, J. Guan, CrystEngComm **12**, 3157 (2010)

84. H. Shimizu, K. Kobayashi, Y. Mizuno, C.A. Randall, J. Am. Ceram. Soc. **97**, 1791 (2014)

85. A. Redinger, S. Siebentritt, Copp. Zinc tin sulfide-based Thin-Film Sol. Cells. **627**, 363 (2015)

86. G.C. Park, T.Y. Seo, C.H. Park, J.H. Lim, J. Joo, Ind. Eng. Chem. Res. **56**, 8235 (2017)

87. B. Li, H. Cao, J. Mater. Chem. **21**, 3346 (2011)

88. A. Ahlawat, P.S. Rana, P.R. Solanki, Mater. Lett. **305**, 130830 (2021)

89. Z. Zhang, C.C. Wang, R. Zakaria, J.Y. Ying, J. Phys. Chem. B. **102**, 10871 (1998). https://doi.org/10.1021/jp982948+

90. T.K. Dhiman, S. Singh, Phys. Status Solidi Appl. Mater. Sci. **216**, 1 (2019)